



OPEN

SUBJECT AREAS:

CONDENSED-MATTER PHYSICS

MATERIALS SCIENCE  
NANOSCIENCE AND TECHNOLOGY

QUANTUM PHYSICS

# Emergence of topological and topological crystalline phases in $\text{TlBiS}_2$ and $\text{TlSbS}_2$

Qingyun Zhang, Yingchun Cheng &amp; Udo Schwingenschlögl

PSE Division, KAUST, Thuwal 23955-6900, Kingdom of Saudi Arabia.

Received  
13 August 2014Accepted  
19 January 2015Published  
11 February 2015

Using first-principles calculations, we investigate the band structure evolution and topological phase transitions in  $\text{TlBiS}_2$  and  $\text{TlSbS}_2$  under hydrostatic pressure as well as uniaxial and biaxial strain. The phase transitions are identified by parity analysis and by calculating the surface states. Zero, one, and four Dirac cones are found for the (111) surfaces of both  $\text{TlBiS}_2$  and  $\text{TlSbS}_2$  when the pressure grows, which confirms trivial-nontrivial-trivial phase transitions. The Dirac cones at the  $\bar{M}$  points are anisotropic with large out-of-plane component.  $\text{TlBiS}_2$  shows normal, topological, and topological crystalline insulator phases under hydrostatic pressure, thus being the first compound to exhibit a phase transition from a topological to a topological crystalline insulator.

Correspondence and requests for materials should be addressed to  
U.S. (Udo.  
Schwingenschlogl@  
kaust.edu.sa)

**T**opological insulators, a new kind of quantum matter with an energy gap in the bulk and an odd number of gapless edge or surface states, have been studied intensively in the last decade<sup>1–4</sup>. Metallic surface states, which originate from spin-orbit coupling, are topologically protected by time-reversal symmetry, making the materials interesting for spintronic and quantum computation applications. Many three dimensional topological insulators have been theoretically predicted and experimentally confirmed<sup>5,6</sup>, including Tl-based III-V-VI<sub>2</sub> ternary chalcogenides<sup>7–15</sup>. Among these compounds,  $\text{TlBiS}_2$  is found to be a trivial semiconductor in experiment, whereas different first principles calculations have predicted it to be either trivial<sup>15</sup> or nontrivial<sup>13</sup>, implying that the topological property is very sensitive to the structural details. It has been reported that  $\text{TlSbS}_2$  can be tuned from a trivial insulator into a topological semimetal by uniaxial strain<sup>13</sup>. In general, strain engineering has been a fruitful path to new topological systems ever since HgTe had been predicted to undergo a phase transition under strain<sup>2</sup>. Various studies have dealt with strain induced topological phase transitions<sup>16–25</sup>.

Lately interest is shifting to the socalled topological crystalline insulators<sup>26,27</sup>, which are different from standard topological insulators in that the gapless surface states are protected by mirror symmetry rather than by time-reversal symmetry. The protection thus persists even when time-reversal symmetry is broken, for example by a magnetic field or magnetic dopant, which strongly broadens the field of potential applications. Topological crystalline insulators are rare, having been confirmed experimentally only for the SnTe class of compounds<sup>28–32</sup> as well as for  $\text{Bi}_2\text{Te}_3$ <sup>33</sup>. To evaluate the physics of topological crystalline insulators, it is therefore essential to search for additional cases where this phase is realized. In the present work we study  $\text{TlBiS}_2$  and  $\text{TlSbS}_2$  by first principles density functional theory and demonstrate that hydrostatic pressure as well as uniaxial and biaxial strain induce topological phase transitions in both systems. For  $\text{TlBiS}_2$  a topological crystalline insulator phase emerges under hydrostatic pressure. The nature of the different phases is confirmed by calculating the surface states.

## Results

$\text{TlBiS}_2$  and  $\text{TlSbS}_2$  have rhombohedral structures with space group  $\bar{R}\bar{3}m$ , which is similar to  $\text{Bi}_2\text{Te}_3$ . There are four atoms per unit cell, with the Tl, Bi/Sb, and S atoms placed in layers normal to the three-fold axis in the sequence – Tl–S–Bi–S–, as shown in Fig. 1(a). Each Tl/Bi layer is sandwiched between two S layers, which results in a strong interlayer coupling so that the crystal structure is essentially three-dimensional. Tl, Bi, and S are located at the (0,0,0), (0.5,0.5,0.5), and ( $\pm u$ ,  $\pm u$ ,  $\pm u$ ) sites, respectively. The structure has inversion symmetry where both Tl and Bi/Sb act as inversion centers. The corresponding hexagonal supercell is shown in Fig. 1(b) and the projections of the bulk Brillouin zone onto the surface Brillouin zones is demonstrated in Fig. 1(c). While hydrostatic pressure by definition is isotropic, the uniaxial strain is applied along the  $z$ -axis and the biaxial strain within the  $xy$ -plane. In no case the symmetry of the system is altered, which simplifies the analysis. The magnitude of the

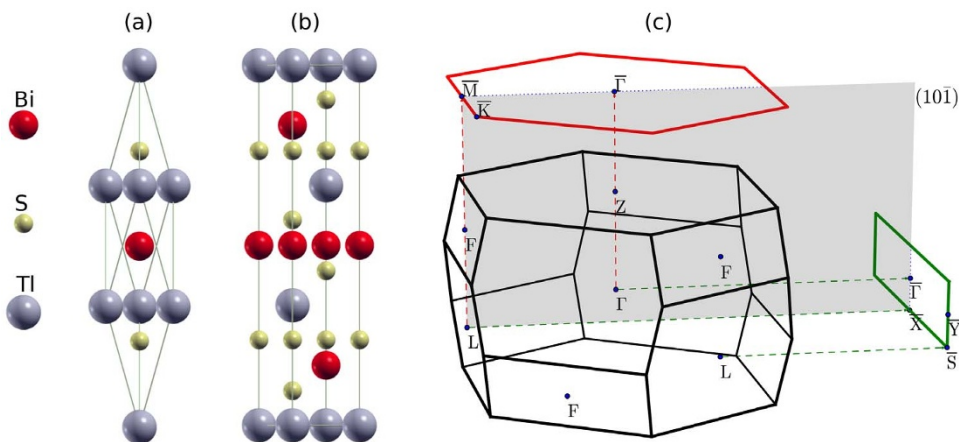


**Figure 1** | (a) Unit cell of  $\text{TlBiS}_2$ , (b) corresponding hexagonal supercell, and (c) three dimensional Brillouin zone with projections onto the surface Brillouin zones.

uniaxial strain is defined as  $\epsilon_z \equiv \frac{c - c_0}{c_0} \times 100\%$  and that of the biaxial strain as  $\epsilon_{xy} \equiv \frac{a - a_0}{a_0} \times 100\%$ , where  $a_0$  and  $c_0$  are the in-plane and out-of-plane equilibrium lattice constants of the hexagonal supercell.

We first study the band structures and topological properties of  $\text{TlBiS}_2$  under strain. Structure relaxations are performed without spin-orbit coupling, yielding the lattice parameters  $a_0 = 7.789 \text{ \AA}$  and angle  $\alpha = 30.9^\circ$ , which are close to the experimental values ( $a_0 = 7.684 \text{ \AA}$ ,  $\alpha = 30.98^\circ$ )<sup>34</sup>. The internal parameter characterizing the positions of the atoms is  $u = 0.237$ . The electronic band structure of  $\text{TlBiS}_2$  under hydrostatic pressure is addressed in Fig. 2. Without strain, see Fig. 2(b), the conduction band minimum and valence band maximum are both located at the  $\Gamma$  point with an energy gap of 7 meV. This value differs from previous calculations<sup>13,15,35</sup>, mainly due to different lattice constants, pseudopotentials, and exchange functionals. Examining the region near the Fermi energy, we find that the electronic properties are sensitive to the pressure. When the pressure increases from  $-2 \text{ GPa}$  to  $8 \text{ GPa}$  the energy gap at the  $\Gamma$  point first closes and then reopens, with a critical pressure around  $0 \text{ GPa}$ . A

similar behavior is found for the  $F$  point, with a critical pressure around  $5 \text{ GPa}$ . The system remains a direct band gap semiconductor up to  $8 \text{ GPa}$ , although the conduction band minimum and valence band maximum move from the  $\Gamma$  to the  $F$  point around  $3 \text{ GPa}$ . The band gaps for  $-2$ ,  $2$ , and  $8 \text{ GPa}$  pressure are  $0.20$ ,  $0.19$ , and  $0.28 \text{ eV}$ , respectively. It is also found that at the conduction and valence band edges move away from the  $\Gamma$  point to the  $\Gamma$ - $F$  line for pressure larger than  $5 \text{ GPa}$ . Finally, up to  $15 \text{ GPa}$  the band gaps at the  $\Gamma$  and  $F$  points are found to grow monotonously.

In Fig. 2 we project the wave functions to atomic orbitals, finding that the states around the Fermi level are mostly contributed by the  $\text{Tl } p$ ,  $\text{Bi } p$ , and  $\text{S } p$  orbitals. In Fig. 2(a) the conduction bands are dominated by the  $\text{Tl}$  and  $\text{Bi } p$  orbitals, whereas the valence bands are dominated by the  $\text{S } p$  orbitals. No band inversion is found, which means that the system is in a trivial phase. In Fig. 2(b) the conduction and valence band edges touch each other and the orbital character switches at the Fermi level, i.e., a band inversion has occurred. In Fig. 2(d), for  $5 \text{ GPa}$  pressure, the conduction and valence bands touch at the  $F$  point and another band inversion occurs. Due to the even number of band inversions at the time-reversal invariant

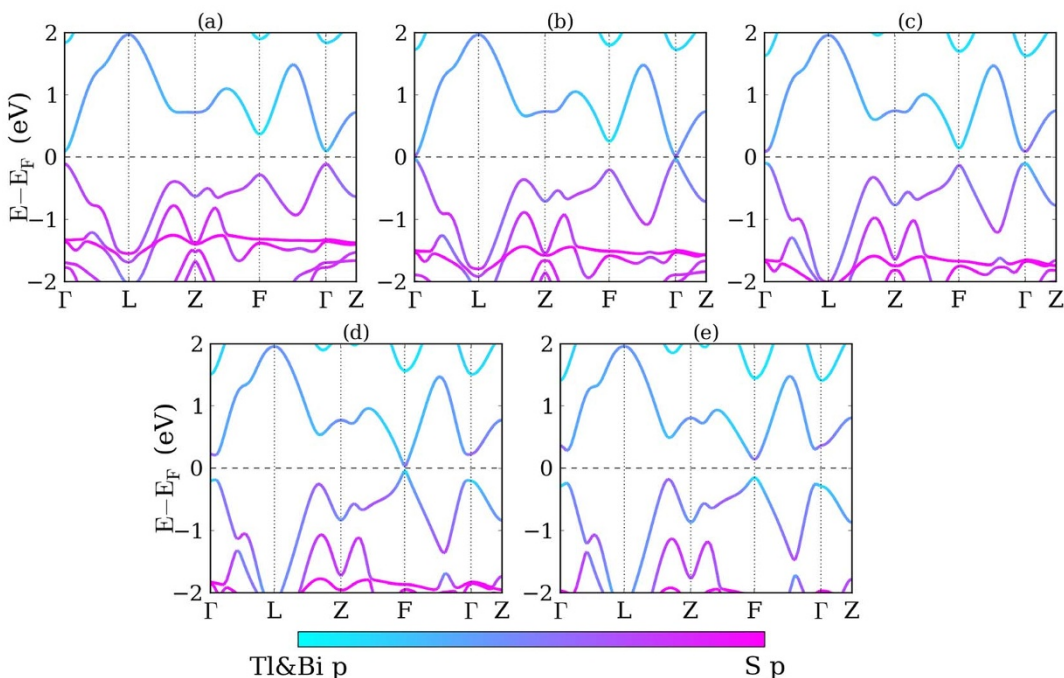


**Figure 2** | Band structures of  $\text{TlBiS}_2$  for (a)  $-2 \text{ GPa}$ , (b)  $0 \text{ GPa}$ , (c)  $2 \text{ GPa}$ , (d)  $5 \text{ GPa}$ , and (e)  $8 \text{ GPa}$  hydrostatic pressure.



momenta the system is back to a trivial phase. The inversion symmetry of  $\text{TiBiS}_2$  allows us to perform a parity analysis. By checking the parities of the valence states at the eight time-reversal invariant momenta ( $1\Gamma$ ,  $3\text{F}$ ,  $1\text{Z}$ , and  $3\text{L}$ ), we find that the topological invariants at  $-2$ ,  $0$ ,  $2$ ,  $5$  and  $8$  GPa pressure are  $(0;000)$ ,  $(1;000)$ ,  $(1;000)$ ,  $(0;000)$ , and  $(0;000)$ , respectively, consistent with the band inversion picture. We notice that the system is topologically nontrivial without strain, which contradicts the experimental result. The possible reason for this difference is the presence of strain in the sample due to the finite temperature, the substrate or other factors.

Band structures for biaxial and uniaxial strain are shown in Fig. 3(b)-(e), which are compared to the band structure without strain in Fig. 3(a). The variations under biaxial strain are very different from those under hydrostatic pressure. For biaxial compression, see Fig. 3(b), the system first changes from a direct gap semiconductor to an indirect gap semiconductor and then to a semimetal. No band inversion is found at the  $\Gamma$  and  $\text{F}$  points. On the other hand, Fig. 3(c) shows for biaxial tension that the energy gap at the  $\Gamma$  point first closes and then reopens. The conduction and valence band edges shift upwards at the  $\text{F}$  point and downwards at the  $\Gamma$  point, i.e., the system changes from a semiconductor to a semimetal. For uniaxial compression, see Fig. 3(d), a band inversion occurs at the  $\Gamma$  point. The system first turns into an indirect gap semiconductor and then into a semimetal. For uniaxial tension, see Fig. 3(e), no band inversion is found and the system remains an indirect gap semiconductor up to  $6\%$  strain. Using parity analysis, we find that the topological invariants are  $(0;000)$ ,  $(1;000)$ ,  $(1;000)$ , and  $(0;000)$  under  $-5\%$ ,  $5\%$  biaxial strain and  $-6\%$ ,  $6\%$  uniaxial strain, respectively.

To confirm the topological phase transitions, we investigate the evolution of the surface states of  $\text{TiBiS}_2$  under hydrostatic pressure. We first obtain a tight-binding Hamiltonian from maximally localized Wannier functions<sup>36</sup> using the WANNIER90 code<sup>37</sup>. A hexagonal supercell with  $8 \times 8 \times 8$   $\text{k}$  points is adopted in the non-self-consistent calculation. The  $\text{Ti}$   $s$ ,  $p$ ,  $\text{Bi}$   $p$ , and  $\text{S}$   $p$  orbitals are used for the initial projection. Once the tight-binding Hamiltonian is established, a slab of 241 atomic layers with (111)-oriented surfaces is built with  $\text{Ti}$  on both the top and bottom surfaces. Calculated band structures near the Fermi level are shown in Fig. 4. Due to the inversion symmetry of

the slab, the bands related to the top and bottom surfaces are degenerate. We project the states near the Fermi level to the first eight atomic layers on the top side of the slab. According to Fig. 4(a), for  $-2$  GPa pressure there is no state in the bulk energy gap and the surface states marked by red circles are buried in bulk states. On the other hand, for  $2$  GPa pressure, see Fig. 4(b), a surface state emerges in the energy gap at the  $\bar{\Gamma}$  point and the Dirac point is located below the Fermi level, i.e., we have a nontrivial phase. For  $8$  GPa pressure, see Fig. 4(c), an additional surface state arises at the  $\bar{M}$  point. Since there are three  $\bar{M}$  points in the surface Brillouin zone, we have a total of four Dirac cones. The even number again reflects a trivial phase. The contributions of the surface layers are highlighted by the size of the red circles. Comparing the surface states at the  $\bar{\Gamma}$  point in Fig. 4(b) and (c), we find that the proportion of the gapless states on the surface layers is determined by the pressure.

In Fig. 5 we show constant energy cuts through the Dirac cones for the  $\bar{\Gamma}$  and  $\bar{M}$  points at  $-0.04$  eV and  $0.02$  eV, respectively. Clearly, the energy contour is anisotropic at the  $\bar{M}$  point with a distortion along the  $\bar{M}-\bar{\Gamma}$  direction. Experimentally, above the Dirac point the spin direction is in-plane and precesses clockwise around the  $\bar{\Gamma}$  point, whereas below it precesses counterclockwise. In strained  $\text{TiBiS}_2$  we find the same property for the surface states. There is also a small  $z$  component with three fold symmetry, which results from the in-plane potential gradients<sup>38</sup>. These findings agree with previous calculations in Ref. 14. It is a distinct feature of the surface states at the  $\bar{M}$  point that the spin amplitudes are different for the  $x$  and  $y$  components. The spin  $z$  component has no three fold symmetry and the amplitude is larger than at the  $\bar{\Gamma}$  point. This larger deviation of the spin vector from the  $xy$ -plane results from the higher in-plane anisotropy at the  $\bar{M}$  point. By fitting the data, we find that the in-plane spin angle  $\theta_s$  obeys the following relations with respect to the azimuthal angle  $\theta$  of the momentum:

$$\bar{\Gamma} : \theta_s \approx -\theta - 90^\circ \quad (1)$$

$$\begin{aligned} \bar{M}_1 : \theta_s \approx & -\theta - 30^\circ + 40.3^\circ \cdot \sin(2\theta - 60^\circ) \\ & + 13.8^\circ \cdot \sin(4\theta + 60^\circ) + 5.7^\circ \cdot \sin(6\theta + 180^\circ) \end{aligned} \quad (2)$$

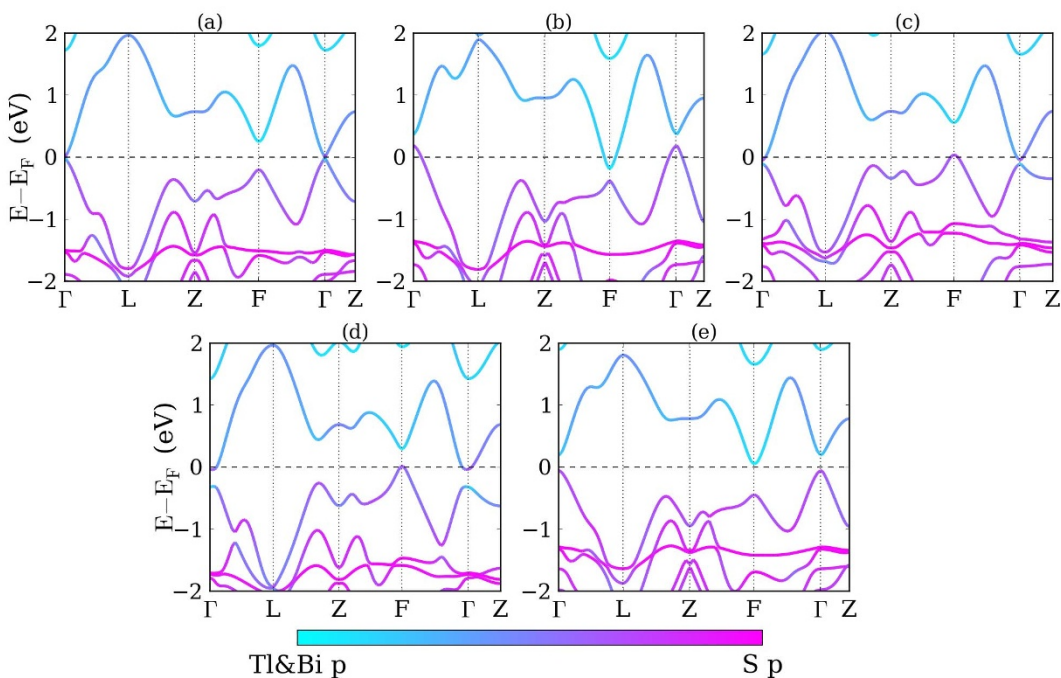


**Figure 3 |** Band structures of  $\text{TiBiS}_2$  (a) without strain, with (b)  $-5\%$ , (c)  $5\%$  biaxial strain as well as (d)  $-6\%$  and (e)  $6\%$  uniaxial strain.

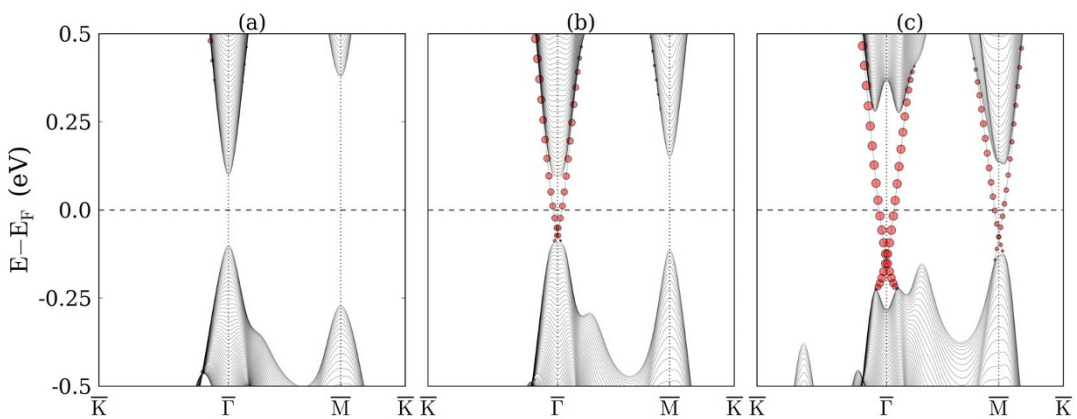


**Figure 4** | Band structures of the TiBiS<sub>2</sub> slab with (111)-oriented surfaces under (a)  $-2$  GPa, (b)  $2$  GPa, and (c)  $5$  GPa pressure. The size of the red circles represents the contribution of the first eight atomic layers.

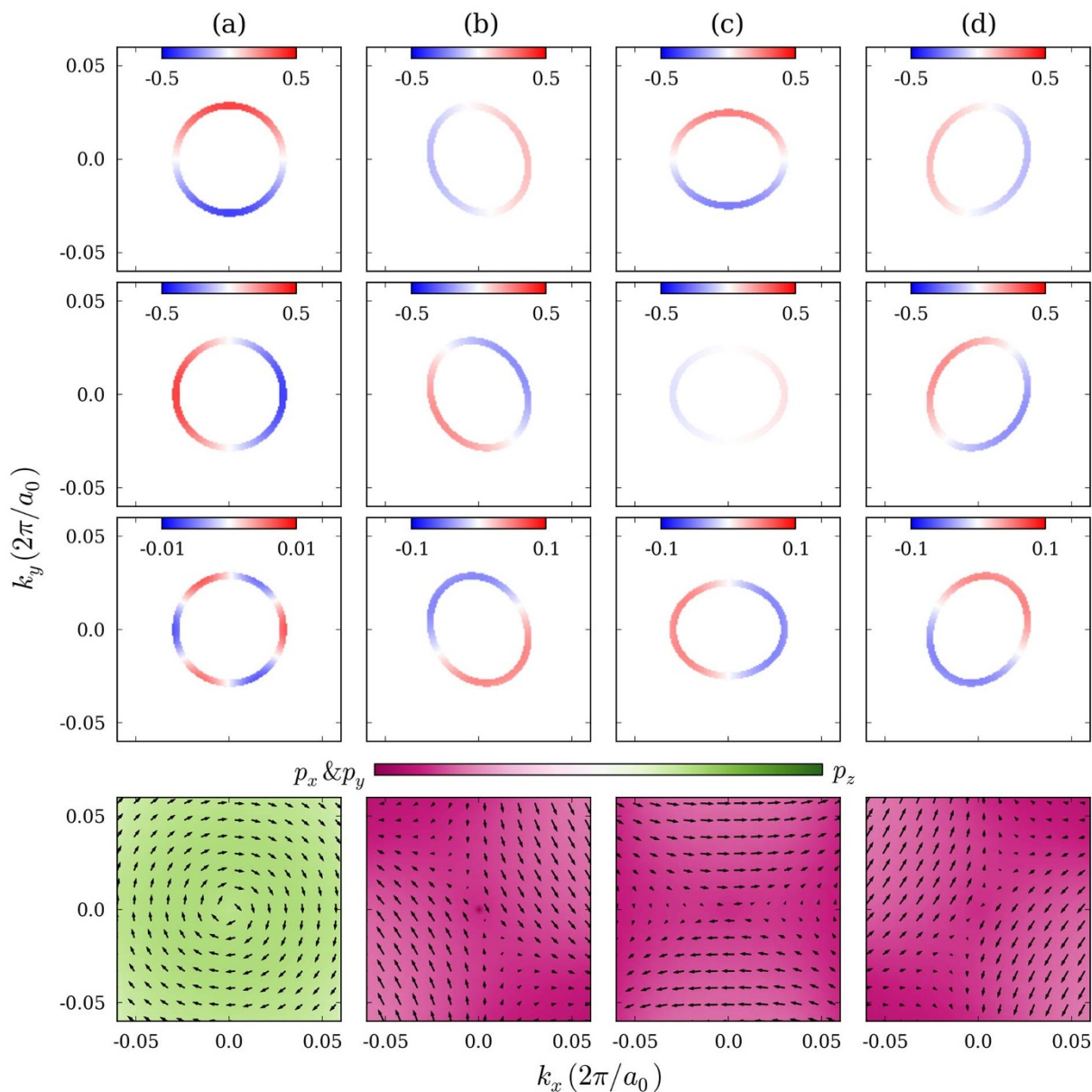


**Figure 5** | Spin polarization and orbital characteristics of the surface states of the TiBiS<sub>2</sub> slab at the (a)  $\bar{\Gamma}$ , (b)  $\bar{M}_1$ , (c)  $\bar{M}_2$ , and (d)  $\bar{M}_3$  points under  $8$  GPa pressure. The first, second and third rows correspond to the spin  $x$ ,  $y$  and  $z$  components at a constant energy. The fourth row shows the in-plane spin vectors and orbital characteristics above the Dirac point.

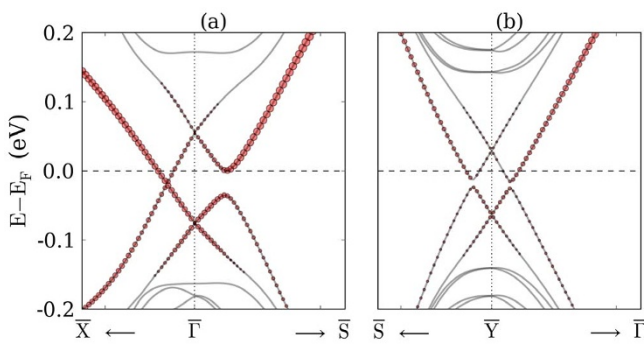


**Figure 6 | Band structure of the TlBiS<sub>2</sub> slab with (121)-oriented surfaces in the vicinity of the (a)  $\bar{\Gamma}$  and (b)  $\bar{Y}$  points.** The slab consists of 90 atomic layers. The size of the red circles represents the contribution of the first three atomic layers.

$$\bar{M}_2 : \theta_s \approx -\theta + 90^\circ - 40.8^\circ \cdot \sin(2\theta) - 13.3^\circ \cdot \sin(4\theta) - 5.9^\circ \cdot \sin(6\theta) \quad (3)$$

$$\begin{aligned} \bar{M}_3 : \theta_s \approx & -\theta - 150^\circ + 40.5^\circ \cdot \sin(2\theta + 60^\circ) \\ & + 13.2^\circ \cdot \sin(4\theta - 60^\circ) + 5.9^\circ \cdot \sin(6\theta + 180^\circ) \end{aligned} \quad (4)$$

The direction of the spin and momentum are related to each other at the  $\bar{\Gamma}$  point, whereas at the  $\bar{M}$  point the spin behaves inversely to the momentum and has a large out-of-phase component, which is due to the anisotropy of the Dirac cone. This relation between spin and momentum can be explained by the spin-orbital texture of the surface states which is also found in Bi<sub>2</sub>Se<sub>3</sub> and Bi<sub>2</sub>Te<sub>3</sub><sup>39,40</sup>. At the  $\bar{\Gamma}$  and  $\bar{M}$  points the surface states are dominated by the out-of-plane  $p_z$  and in-plane  $p_x, p_y$  orbitals, respectively.

Topological crystalline insulators are characterized by a non-zero mirror Chern number. Therefore, mirror symmetry protected Dirac cones arise in the surface electronic structure. Similarity between the surface states of TlBiS<sub>2</sub> and SnTe, compare Refs. 28–32, 41, 42, implies that TlBiS<sub>2</sub> becomes a topological crystalline insulator at 8 GPa pressure. To confirm this conjecture, we study the bands of the (121) surface of TlBiS<sub>2</sub>, see Fig. 6, which is symmetrical about the

(101) mirror plane. Figure 1(c) demonstrates that the (101) mirror plane crosses the surface Brillouin zone along the line  $\bar{\Gamma}-\bar{X}$  and that the  $\bar{\Gamma}$  point as well as one of the F points of the bulk Brillouin zone are projected onto the  $\bar{\Gamma}$  point. Since the band structure in Fig. 2(e) shows band inversion at both the  $\bar{\Gamma}$  and F points, we reproduce the general situation of Ref. 41 and expect the projected Dirac cones to hybridize at their intersection. This expectation is confirmed by Fig. 6(a), which shows that the hybridization opens an energy gap at the Fermi level, except for the mirror-symmetric line  $\bar{\Gamma}-\bar{X}$ . Along this line a descendent Dirac cone is created due to protection by mirror symmetry (rather than by time-reversal symmetry). At the  $\bar{Y}$  point, see Fig. 6(b), the hybridization leads to an energy gap, because the two F points that are projected onto this point do not lie on the (101) mirror plane<sup>42</sup>. To the best of our knowledge, TlBiS<sub>2</sub> is the first reported compound which can be tuned from a topological insulator into a topological crystalline insulator by applying hydrostatic pressure.

For TlSbS<sub>2</sub> without strain we obtain the lattice parameters  $a_0 = 7.758 \text{ \AA}$  and  $\alpha = 30.3^\circ$  as well as the internal parameter  $u = 0.236$ . Without strain, see Fig. 7(a), we obtain a direct gap semiconductor with an energy gap of 0.128 eV at the  $\bar{\Gamma}$  point. When the pressure increases from 0 GPa to 8 GPa the energy gaps at the  $\bar{\Gamma}$  and F points first close and then reopen, similar to TlBiS<sub>2</sub>. The critical pressures for closure are around 2 and 5 GPa for the  $\bar{\Gamma}$  and F points, respectively. Distinctly different to TlBiS<sub>2</sub>, under pressure the valence band edge at the  $\bar{\Gamma}$  point shifts upwards and the conduction band edge at the F point downwards, which makes the system change from a semiconductor to a semimetal. Similar to TlBiS<sub>2</sub>, the states around the Fermi level are mostly due to the Tl  $p$ , Sb  $p$ , and S  $p$  orbitals. In Fig. 7(a) we find no band inversions at the time-reversal invariant momenta and the conduction bands are dominated by the Tl and Sb  $p$  orbitals, while the valence bands are dominated by the S  $p$  orbitals. In Fig. 7(b) a band inversion occurs at the  $\bar{\Gamma}$  point, i.e., the system changes from a trivial phase into a nontrivial phase. For 5 GPa pressure, see Fig. 7(d), the conduction and valence band edges touch at the F point and another band inversion occurs, transforming the system from a topological semimetal into a trivial semimetal. By parity analysis, we find that the topological invariants without pres-

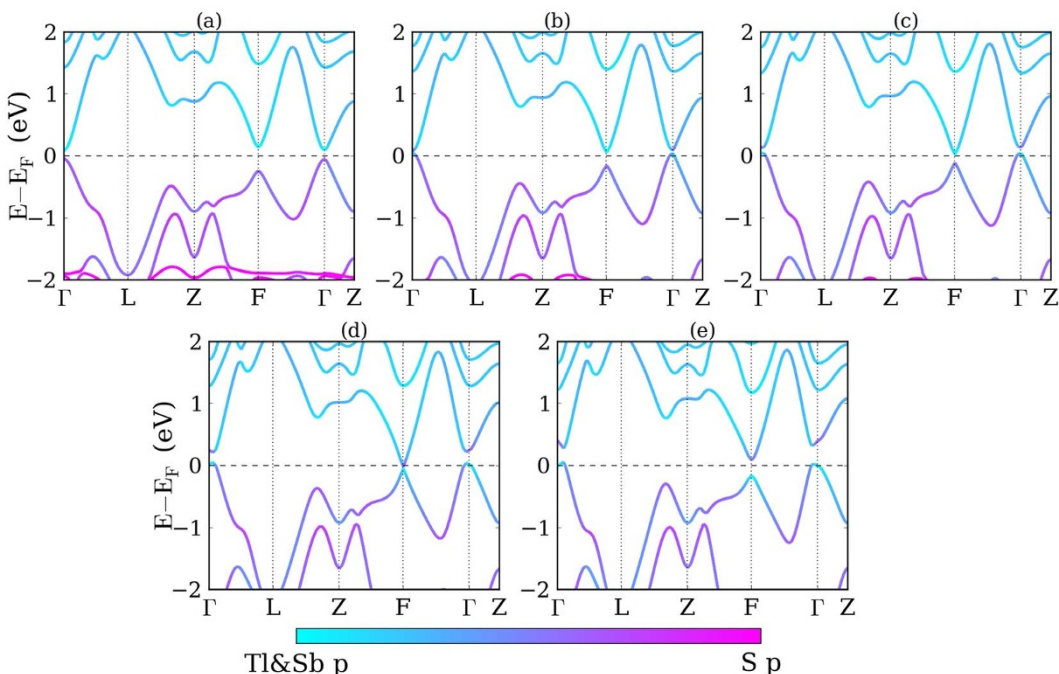


**Figure 7 | Band structures of TlSbS<sub>2</sub> for (a) 0 GPa, (b) 2 GPa, (c) 3 GPa, (d) 5 GPa, and (e) 8 GPa hydrostatic pressures.**

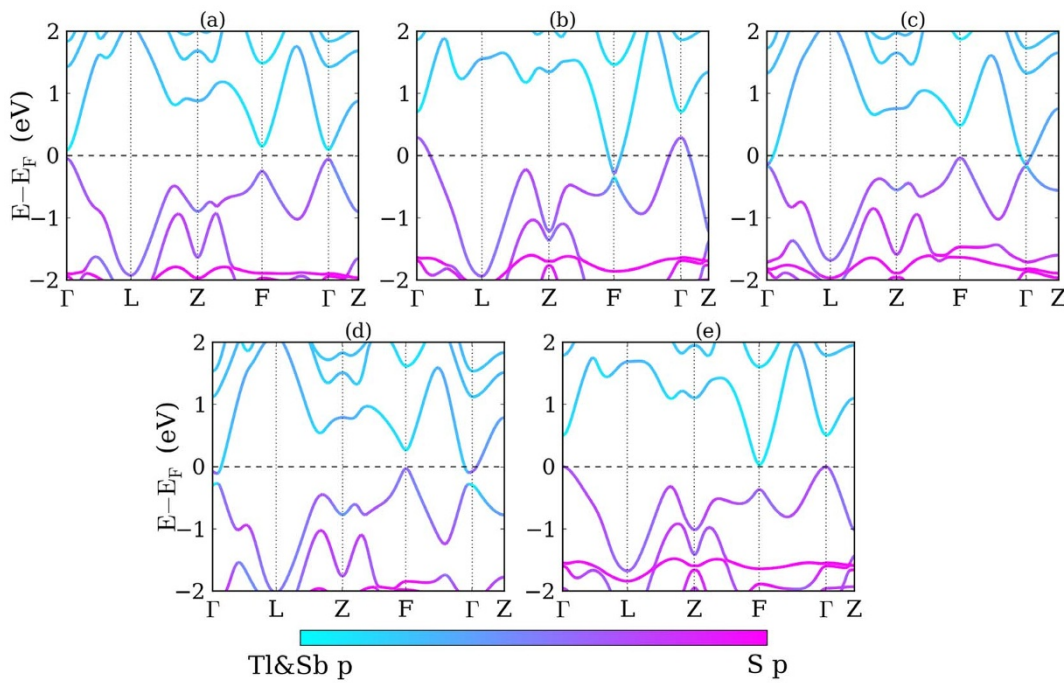


**Figure 8 |** Band structures of  $\text{TlSbS}_2$  (a) without strain, with (b)  $-5\%$ , (c)  $5\%$  biaxial strains as well as (d)  $-6\%$ , and (e)  $6\%$  uniaxial strains.

sure and under  $2$ ,  $3$ ,  $5$ , and  $8$  GPa pressure are  $(0;000)$ ,  $(1;000)$ ,  $(1;000)$ ,  $(0;000)$ , and  $(0;000)$ , respectively.

Band structures under biaxial and uniaxial strain are illustrated in Fig. 8(b)–(e). For comparison, the band structure without strain is shown in Fig. 8(a). For biaxial compression, see Fig. 8(b), the system transforms from a direct gap semiconductor into a semimetal with the valence band maximum and conduction band minimum located at the  $\Gamma$  and  $F$  point, respectively. A band inversion occurs at the  $F$  point and the energy gap at the  $\Gamma$  point grows. According to Fig. 8(c), under biaxial tension the variation of the band structure near the Fermi level is reversed as compared to compression. We observe that at the  $F$  point the conduction and valence band edges shift upwards and the energy gap grows, whereas at the  $\Gamma$  point the band edges shift downwards and touch at  $5\%$  tension. For uniaxial compression, see Fig. 8(d), the system changes from a direct gap semiconductor into a semimetal with a band inversion at the  $\Gamma$  point, whereas for uniaxial tension in Fig. 8(e) it first changes from a direct gap semiconductor into an indirect gap semiconductor and then into a semimetal. The band gaps at the  $\Gamma$  and  $F$  points both grow and no band inversion appears. By parity analysis, we obtain the topological invariants

$(1;000)$ ,  $(1;000)$ ,  $(1;000)$ , and  $(0;000)$  under  $-5\%$ ,  $5\%$  biaxial strain, and  $-6\%$ ,  $6\%$  uniaxial strain, respectively.

The surface states are studied analogously to  $\text{TLBiS}_2$ . Without strain, see Fig. 9(a), there is no surface state in the bulk energy gap, i.e., the system is a trivial semiconductor, whereas under  $3$  GPa pressure, see Fig. 9(b), a surface state emerges in the energy gap at the  $\bar{\Gamma}$  point above the Fermi level. The system is in a nontrivial phase and the Dirac cone is buried in bulk states. Under  $8$  GPa pressure, see Fig. 9(c), an additional surface state arises at the  $\bar{M}$  point, located at the Fermi level, but still buried in bulk states.  $\text{TLBiS}_2$  under  $8$  GPa pressure is a topological crystalline semimetal. Due to the semimetallic nature, the surface states here are less interesting than for  $\text{TLBiS}_2$ , although the spin-orbital textures of the Dirac cones are similar.

## Discussion

We have studied the topological properties of  $\text{TLBiS}_2$  and  $\text{TLBiS}_2$  under strain. Two topological phase transitions occur in both systems under hydrostatic pressure.  $\text{TLBiS}_2$  remains a direct gap semiconductor up to  $8$  GPa, while  $\text{TLBiS}_2$  turns from a semiconductor

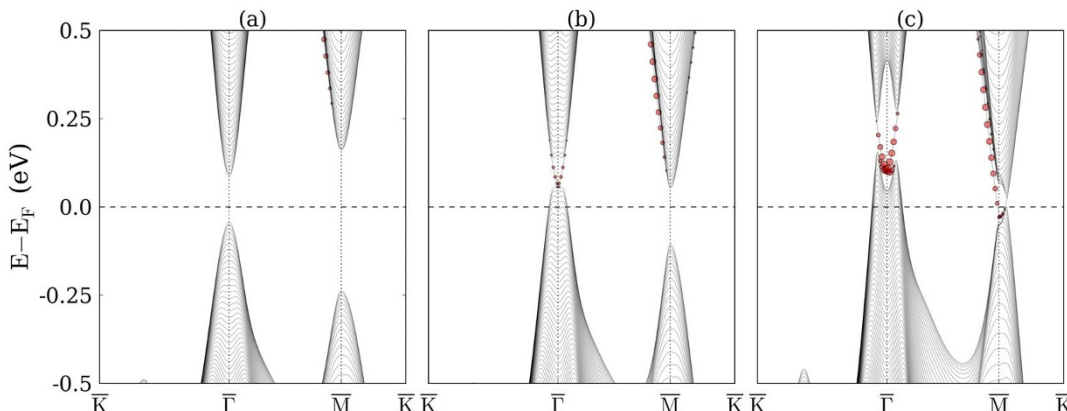


**Figure 9 |** Band structures of the  $\text{TLBiS}_2$  slab under (a)  $0$  GPa, (b)  $3$  GPa, and (c)  $5$  GPa pressure. The size of the red circles represents the contribution of the surface layer.



into a semimetal. Biaxial and uniaxial strain also drive topological phase transitions. Band structures of slabs with (111)-oriented surfaces show that a surface state emerges at the  $\bar{\Gamma}$  point when the system is in the topological regime. For pressure larger than 5 GPa another surface state appears at the  $\bar{M}$  point, transforming the system from a nontrivial into a trivial phase. By further investigating the states on the  $(\bar{1}2\bar{1})$  surface, which are symmetric about the  $(10\bar{1})$  mirror plane, we find that  $\text{TLBiS}_2$  under 8 GPa pressure undergoes a phase transition from a topological to a topological crystalline insulator. Similar transitions can also be expected for other Tl-based III-V-VI<sub>2</sub> ternary chalcogenides, for example  $\text{TLBiTe}_2$ . The surface states induced by strain should be investigated by spin- and angle-resolved photoemission spectroscopy to confirm our predictions.

## Methods

Our calculations are based on the Quantum ESPRESSO code<sup>43</sup>, using the generalized gradient approximation for the exchange-correlation functional and norm-conserving pseudopotentials. A kinetic energy cutoff of 680 eV and a  $10 \times 10 \times 10$  k-point mesh are employed.

1. Kane, C. L. & Mele, E. J. Z<sub>2</sub> topological order and the quantum spin Hall effect. *Phys. Rev. Lett.* **95**, 146802 (2005).
2. Fu, L. & Kane, C. L. Topological insulators with inversion symmetry. *Phys. Rev. B* **76**, 045302 (2007).
3. Hasan, M. Z. & Kane, C. L. Topological insulators. *Rev. Mod. Phys.* **82**, 3045–3076 (2010).
4. Qi, X.-L. & Zhang, S.-C. Topological insulators and superconductors. *Rev. Mod. Phys.* **83**, 1057–1110 (2011).
5. Yan, B. H. & Zhang, S.-C. Topological materials. *Rep. Prog. Phys.* **75**, 096501 (2012).
6. Feng, W. X. & Yao, Y. G. Three-dimensional topological insulators: A review on host materials. *Sci. China Phys. Mech. Astron.* **55**, 2199 (2012).
7. Kuroda, K. *et al.* Experimental realization of a three-dimensional topological insulator phase in ternary chalcogenide  $\text{TLBiSe}_2$ . *Phys. Rev. Lett.* **105**, 146801 (2010).
8. Chen, Y. L. *et al.* Single Dirac cone topological surface state and unusual thermoelectric property of compounds from a new topological insulator family. *Phys. Rev. Lett.* **105**, 266401 (2010).
9. Sato, T. *et al.* Unexpected mass acquisition of Dirac fermions at the quantum phase transition of a topological insulator. *Nat. Phys.* **7**, 840–844 (2011).
10. Xu, S.-Y. *et al.* Topological phase transition and texture inversion in a tunable topological insulator. *Science* **332**, 560–564 (2011).
11. Souma, S. *et al.* Spin polarization of gapped Dirac surface states near the topological phase transition in  $\text{TLBi}(\text{S}_{1-x}\text{Se}_x)_2$ . *Phys. Rev. Lett.* **109**, 186804 (2012).
12. Lin, H. *et al.* Single-Dirac-cone topological surface states in the  $\text{TLBiSe}_2$  class of topological semiconductors. *Phys. Rev. Lett.* **105**, 036404 (2010).
13. Yan, B. H. *et al.* Theoretical prediction of topological insulators in thallium-based III-V-VI<sub>2</sub> ternary chalcogenides. *Europhys. Lett.* **90**, 37002 (2010).
14. Eremeev, S. V. *et al.* Ab initio electronic structure of thallium-based topological insulators. *Phys. Rev. B* **83**, 205129 (2011).
15. Singh, B. *et al.* Topological electronic structure and Weyl semimetal in the  $\text{TLBiSe}_2$  class of semiconductors. *Phys. Rev. B* **86**, 115208 (2012).
16. Feng, W. *et al.* Strain tuning of topological band order in cubic semiconductors. *Phys. Rev. B* **85**, 195114 (2012).
17. Winterfeld, L. *et al.* Strain-induced topological insulator phase transition in  $\text{HgSe}$ . *Phys. Rev. B* **87**, 075143 (2013).
18. Agapito, L. A., Kioussis, N., Goddard III, W. A. & Ong, N. P. Novel family of chiral-based topological insulators: elemental tellurium under strain. *Phys. Rev. Lett.* **110**, 176401 (2013).
19. Zhang, Q., Cheng, Y. & Schwingenschlögl, U. Series of topological phase transitions in  $\text{TiTe}_2$  under strain. *Phys. Rev. B* **88**, 155317 (2013).
20. Bahramy, M., Yang, B.-J., Arita, R. & Nagaosa, N. Emergence of non-centrosymmetric topological insulating phase in  $\text{BiTeI}$  under pressure. *Nat. Commun.* **3**, 679 (2012).
21. Zhu, Z. Y., Cheng, Y. C. & Schwingenschlögl, U. Topological phase transition in layered  $\text{GaS}$  and  $\text{GaSe}$ . *Phys. Rev. Lett.* **108**, 266805 (2012).
22. Sun, Y. *et al.* Strain-driven onset of nontrivial topological insulating states in Zintl  $\text{Sr}_2\text{X}$  compounds (X = Pb, Sn). *Phys. Rev. B* **84**, 165127 (2011).
23. Sun, Y., Chen, X.-Q., Yunoki, S., Li, D. & Li, Y. New family of three-dimensional topological insulators with antiperovskite structure. *Phys. Rev. Lett.* **105**, 216406 (2010).
24. Young, S. M. *et al.* Theoretical investigation of the evolution of the topological phase of  $\text{Bi}_2\text{Se}_3$  under mechanical strain. *Phys. Rev. B* **84**, 085106 (2011).
25. Sa, B., Zhou, J., Song, Z., Sun, Z. & Ahuja, R. Pressure-induced topological insulating behavior in the ternary chalcogenide  $\text{Ge}_2\text{Sb}_2\text{Te}_5$ . *Phys. Rev. B* **84**, 085130 (2011).
26. Teo, J. C. Y., Fu, L. & Kane, C. L. Surface states and topological invariants in three-dimensional topological insulators: Application to  $\text{Bi}_{1-x}\text{Sb}_x$ . *Phys. Rev. B* **78**, 045426 (2008).
27. Fu, L. Topological crystalline insulators. *Phys. Rev. Lett.* **106**, 106802 (2011).
28. Hsieh, T. H. *et al.* Topological crystalline insulators in the SnTe material class. *Nat. Commun.* **3**, 982 (2012).
29. Tanaka, Y. *et al.* Experimental realization of a topological crystalline insulator in SnTe. *Nat. Phys.* **8**, 800 (2012).
30. Dziawa, P. *et al.* Topological crystalline insulator states in  $\text{Pb}_{1-x}\text{Sn}_x\text{Se}$ . *Nat. Mater.* **11**, 1023 (2012).
31. Xu, S.-Y. *et al.* Observation of a topological crystalline insulator phase and topological phase transition in  $\text{Pb}_{1-x}\text{Sn}_x\text{Te}$ . *Nat. Commun.* **3**, 1192 (2012).
32. Wojek, B. M. *et al.* Spin-polarized (001) surface states of the topological crystalline insulator  $\text{Pb}_{0.73}\text{Sn}_{0.27}\text{Se}$ . *Phys. Rev. B* **87**, 115106 (2013).
33. Rauch, T., Flieger, M., Henk, J., Mertig, I. & Ernst, A. Dual topological character of chalcogenides: theory for  $\text{Bi}_2\text{Te}_3$ . *Phys. Rev. Lett.* **112**, 016802 (2014).
34. Özer, M., Paraskevopoulos, K. M., Anagnostopoulos, A. N., Kokou, S. & Polychroniadis, E. K. Large single-crystal growth and characterization of the narrow-gap semiconductor  $\text{TLBiS}_2$ . *Semicond. Sci. Technol.* **11**, 1405 (1996).
35. Hoang, K. & Mahanti, S. D. Atomic and electronic structures of thallium-based III-V-VI<sub>2</sub> ternary chalcogenides: Ab initio calculations. *Phys. Rev. B* **77**, 205107 (2008).
36. Marzari, N. & Vanderbilt, D. Maximally localized generalized Wannier functions for composite energy bands. *Phys. Rev. B* **56**, 12847 (1997).
37. Mostofi, A. A. *et al.* wannier90: A tool for obtaining maximally-localised Wannier functions. *Comput. Phys. Commun.* **178**, 685 (2008).
38. Prempér, J., Trautmann, M., Henk, J. & Bruno, P. Spin-orbit splitting in an anisotropic two-dimensional electron gas. *Phys. Rev. B* **76**, 073310 (2007).
39. Cao, Y. *et al.* Mapping the orbital wavefunction of the surface states in three-dimensional topological insulators. *Nat. Phys.* **9**, 499–504 (2013).
40. Zhang, H.-J., Liu, C.-X. & Zhang, S.-C. Spin-orbital texture in topological insulators. *Phys. Rev. Lett.* **111**, 066801 (2013).
41. Liu, J., Duan, W. & Fu, L. Two types of surface states in topological crystalline insulators. *Phys. Rev. B* **88**, 241303(R) (2013).
42. Safaei, S., Kacmar, P. & Buczek, R. Topological crystalline insulator ( $\text{Pb},\text{Sn}$ )Te: Surface states and their spin polarization. *Phys. Rev. B* **88**, 045305 (2013).
43. Giannozzi, P. *et al.* QUANTUM ESPRESSO: a modular and open-source software project for quantum simulations of materials. *J. Phys.: Condens. Matter* **21**, 395502 (2009).

## Acknowledgments

Research reported in this publication was supported by the King Abdullah University of Science and Technology (KAUST). Computational resources have been provided by KAUST IT.

## Author contributions

Q.Y.Z. performed the calculations. Y.C.C. and U.S. contributed to the analysis. All authors wrote the manuscript.

## Additional information

**Competing financial interests:** The authors declare no competing financial interests.

**How to cite this article:** Zhang, Q., Cheng, Y. & Schwingenschlögl, U. Emergence of topological and topological crystalline phases in  $\text{TLBiS}_2$  and  $\text{TLBiSe}_2$ . *Sci. Rep.* **5**, 8379; DOI:10.1038/srep08379 (2015).



This work is licensed under a Creative Commons Attribution 4.0 International License. The images or other third party material in this article are included in the article's Creative Commons license, unless indicated otherwise in the credit line; if the material is not included under the Creative Commons license, users will need to obtain permission from the license holder in order to reproduce the material. To view a copy of this license, visit <http://creativecommons.org/licenses/by/4.0/>